

# Noise of supercontinuum sources in spectral domain optical coherence tomography

MIKKEL JENSEN,<sup>1</sup> IVÁN BRAVO GONZALO,<sup>1</sup> RASMUS DYBBRO ENGELSHOLM,<sup>1</sup> MICHAEL MARIA,<sup>1,2,3</sup> NIELS MØLLER ISRAELSEN,<sup>1</sup> ADRIAN PODOLEANU,<sup>2</sup> AND OLE BANG<sup>1,3,\*</sup>

<sup>1</sup>*DTU Fotonik, Department of Photonics Engineering, Technical University of Denmark, Ørsteds Plads 343, 2800 Kongens Lyngby, Denmark*

<sup>2</sup>*School of Physical Sciences, University of Kent, CT2 7NH, Canterbury, England*

<sup>3</sup>*NKT Photonics A/S, Blokken 84, 3460 Birkerød, Denmark*

\* [oban@fotonik.dtu.dk](mailto:oban@fotonik.dtu.dk)

**Abstract:** In this paper, we investigate the effect of pulse-to-pulse fluctuations of supercontinuum sources on the noise in spectral domain optical coherence tomography (OCT) images. The commonly quoted theoretical expression for the OCT noise is derived for a thermal light source, which is not suitable if a supercontinuum light source is used. We therefore propose a new, measurement-based OCT noise model that predicts the noise without any assumptions on the type of light source. We show that the predicted noise values are in excellent agreement with the measured values. The spectral correlation evaluated for the photodetected signal when using a supercontinuum determines the shape of the OCT noise floor, which must be taken into account when characterizing the sensitivity roll-off of a supercontinuum-based OCT system. The spectral correlations using both conventional supercontinuum sources and low-noise all-normal dispersion supercontinuum sources are investigated, and the fundamental physical effects that cause these correlations are discussed.

## 1. Introduction

Optical coherence tomography (OCT) is a non-invasive imaging technique that relies on white light interferometry to create volumetric images of an investigated sample, which is often biological [1]. The spectral characteristics of the employed light source are central in designing the OCT system, whose axial resolution is inversely proportional to the optical bandwidth of the employed source and directly proportional to the central wavelength squared, and in addition, the optical properties of the sample depend on the central wavelength too. For these reasons exactly, supercontinuum sources are increasingly applied in OCT due to their octave-spanning, high-power spectra covering the visible and near-infrared spectral regions, which allow great freedom in tunability by filtering, both in terms of bandwidth and central wavelength [2–5]. However, most commercially available supercontinuum sources generate broadband light by non-linear amplification of quantum noise as well as strongly phase and amplitude dependent non-linear interactions between optical solitons. Consequently, the supercontinuum sources are inherently noisy [6–8], as opposed to other common OCT sources, e.g., super-luminescent diodes (SLDs). This often forces researchers and clinicians to compromise between ultra-high resolution and shot noise limited imaging. In order to optimize this compromise, both the resolution and the noise should be correctly assessed. The expected resolution is easily predicted using the bandwidth and central wavelength values of the source used, but the noise properties are more complex to quantify. The noise contribution is often split into four terms: read-out noise, dark noise, shot noise, and excess photon noise [9]. While there is a vast amount of literature on noise, most theoretical descriptions implicitly assume that the light source is thermal or pseudo-thermal [10–12], in which case the excess photon noise is evaluated based on a Bose-Einstein distribution for the photon counting distribution.

For supercontinuum sources, this assumption is questionable at best, but for SLDs, which are very common in OCT, the expression can be corrected by introducing an empirical noise suppression factor,  $f$ , which takes into account the amplified spontaneous emission, to reduce the excess noise term:  $\sigma_{ex,SLD}^2 = \sigma_{ex,spont}^2/f$ , where  $\sigma_{ex,SLD}^2$  and  $\sigma_{ex,spont}^2$  are the excess photon noise terms for an SLD and for a spontaneous source, respectively [13]. Supercontinuum sources generate the broadband spectrum in a fundamentally different way than in SLDs or thermal light sources, and a correct expression for the excess photon noise can therefore not be created by another modification of the known formula.

In this work, we derive a general expression for the excess noise based on the measured noise and demonstrate that this predicts the experimental OCT noise figures better than the old model. We further show that the OCT noise floor is not flat along depth and that its shape is determined by the spectral coherence between different wavelength components of a single pulse of the supercontinuum. Both conventional, soliton-based supercontinuum and an all-normal dispersion (ANDi) supercontinuum sources are investigated. Finally, we discuss the sensitivity roll-off of spectral domain (SD)-OCT using a supercontinuum source and how this is affected by noise.

## 2. Theory of noise in optical coherence tomography

In SD-OCT, the broadband light is sent to a Michelson interferometer with the two arms denoted as a reference arm and a sample arm as shown in Fig. 1.

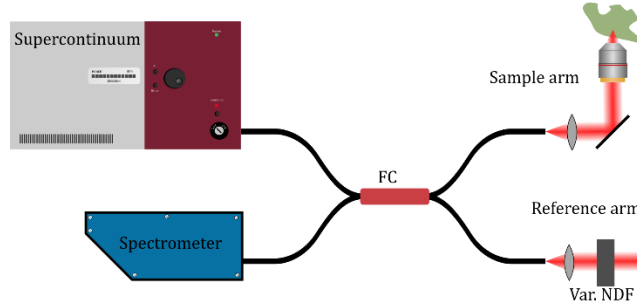


Fig. 1. Sketch of an SD-OCT system. FC is a 50/50 fiber coupler, and NDF is a variable neutral density filter.

A mirror is placed in the reference arm, and the sample is placed in the sample arm. The returning light from the two arms is collected in the output arm of the interferometer, where it is detected by a spectrometer. We will therefore treat the noise at the spectrometer level, measured as the variance of counts in a single pixel. The total noise,  $\sigma_{tot}^2$ , is:

$$\sigma_{tot}^2 = \sigma_{r+d}^2 + \sigma_{shot}^2 + \sigma_{ex}^2, \quad (1)$$

where  $\sigma_{r+d}^2$  is the combined read-out and dark noise of the camera including digitization errors,  $\sigma_{shot}^2[i] = \eta(P_{ref}[i] + P_{sam}[i])\tau_i/(\hbar\omega[i](\Delta e)^2)$  is the shot noise, and  $\sigma_{ex}^2[i] = (\sigma_p[i]\eta\tau_i/(\hbar\omega[i]\Delta e))^2$  is the excess photon noise. In these expressions,  $\eta$  is the combined quantum efficiency of the grating based spectrometer and of the detector array,  $\tau_i$  is the integration time of the spectrometer,  $P_{ref/sam}[i]$  is the power returned from the reference and sample arm, respectively, with incidence on pixel  $i$ ,  $\hbar$  is the reduced Plank constant,  $\omega[i]$  is the angular frequency of the light incident on pixel  $i$ , and  $\Delta e$  is the dimensionless gain factor of the spectrometer converting photo-electrons into counts at the spectrometer output.  $\sigma_p[i]$  is the root mean square (RMS) error of the power incident on pixel  $i$ . The combined read-out and dark noise component represents electronic noise independent of the optical power. The shot noise is the variation of detected power due to the quantization of photons and is thus also present in the absence of any power fluctuations. Finally, the excess photon noise term describes the actual

variations of the incident power. The power fluctuations can be measured experimentally and are typically specified in a normalized fashion as the relative intensity noise (RIN),

$$RIN[i] = \frac{\sigma_p[i]}{\mu_p[i]} = \frac{\sigma_p[i]}{P_{ref}[i] + P_{sam}[i]}, \quad (2)$$

where  $\mu_p[i]$  is the mean power at pixel  $i$ . Inserting  $\sigma_p$  in  $\sigma_{ex}$ , gives

$$\sigma_{ex}^2[i] = \left( \frac{RIN[i](P_{ref}[i] + P_{sam}[i])\eta\tau_i}{\hbar\omega[i]\Delta e} \right)^2, \quad (3)$$

The measured noise includes all three noise terms in Eq. (1), so in order to maximize the excess photon noise contribution to the overall noise, measurements need to be done at high power levels where the excess photon noise dominates due to its square dependence on optical power. Introducing  $N_c = (P_{ref}[i] + P_{sam}[i])\eta\tau_i/(\hbar\omega[i]\Delta e)$  as the expected number of counts within an integration time simplifies the expressions for the shot noise and excess photon noise, which now read,  $\sigma_{shot}^2[i] = N_c/\Delta e$ , and  $\sigma_{ex}^2[i] = RIN[i]^2 N_c^2$ , respectively. The RIN is typically measured with a narrowband filter placed before a fast photodiode connected to an oscilloscope [14,15], but it can just as well be done using a spectrometer, by recording several spectra. When measuring the RIN, care must be taken regarding the hardware for two separate reasons: Firstly, the bandwidth in which  $\mu_p$  and  $\sigma_p$  are measured affects the result in general and in particular for the supercontinuum source because of its non-trivial spectral composition. A wider bandwidth, be it filter bandwidth or spectral resolution of a spectrometer, will, due to averaging effects within the bandwidth, decrease the measured RIN, because spectral components separated by more than 0.1 to 1 nm are uncorrelated for a conventional supercontinuum [16]. The decrease of the RIN with increasing bandwidth is expected to be linear according to the photocounting statistics applied to a thermal source. However, experiments for a supercontinuum show a highly non-linear dependence, and a 3 dB increase has been reported when decreasing the bandwidth from 8 nm to 1 nm [16]. The effect of this correlation of spectral components, or lack thereof, on the OCT noise will be treated in a later section. Secondly, averaging  $M$  pulses in a single read-out decreases the measured RIN, again due to averaging effects, which is why high repetition rate supercontinuum sources show great promise for OCT imaging [17]. Far from the edges of the supercontinuum spectrum, the RIN is well approximated by Gaussian statistics [15,18], and the observed variance will therefore decrease linearly with  $M$ . Therefore, the exact effect of supercontinuum excess noise in SD-OCT must be evaluated using the pixel bandwidth and  $M$ , the number of pulses per integration time of the spectrometer employed. This can be achieved by measuring with the intended hardware or by estimation from RIN measurements performed with different equipment. The excess noise is thus

$$\sigma_{ex}^2[i] = RIN_M[i]^2 N_c[i]^2 = RIN_1[i]^2 N_c[i]^2 / f_{rep} \tau_i, \quad (4)$$

with  $M = f_{rep} \tau_i$ , where  $f_{rep}$  is the repetition rate of the supercontinuum. This formally states what is generally accepted by the scientific community [2,3,17,19]: that the SC excess noise is reduced by increasing either the repetition rate or the integration time.

We now compare the expression given by the measurement-based model with that of the old model. The excess noise contribution from continuous wave thermal or pseudothermal sources reads, for  $\tau_c \ll \tau_i$  [10]:

$$\sigma[i]_{ex,spn}^2 = N_c[i]^2 \tau_c / \tau_i, \quad (5)$$

where  $\tau_c = 1/\Delta\nu = \lambda[i]^2 / (c\delta\lambda)$  is the coherence time of the light that is incident on a single pixel assuming a top-hat spectral shape at each pixel [20].  $c$  is the speed of light in vacuum, and  $\delta\lambda$  is the bandwidth intercepted by a single pixel on the camera. This increase of the coherence time from the fs regime in the total supercontinuum to the ps regime on a single pixel is due to the intrinsic delay caused by the diffraction grating [21]. Disregarding the fact that the assumption of thermal light does not hold for supercontinuum sources, we apply the formula to supercontinua and compare it to our measurement-based model in Eq. (4) in order

to estimate the error. The pulsed nature of supercontinua requires the duty cycle to be taken into account [22], such that the expression reads:

$$\sigma_{ex,spen}^2 = N_c[i]^2 \tau_c / (\tau_i f_{rep} \tau_p), \quad (6)$$

where  $\tau_p$  is the pulse length. Comparing this to  $\sigma_{ex}^2[i]$  in Eq. (4), reveals that the old model predicts  $RIN_1[i]^2 = \tau_c / \tau_p$ .

### 3. Results and discussion

In order to validate the measurement-based noise model and compare it to the old noise model, an SD-OCT system with the sample arm blocked is used to obtain a series of 1024 spectra at 33 different power levels, which were manually adjusted with a variable neutral density filter. The blocked sample arm imitates the case when the sample arm reflectivity is much less than that in the reference arm, which is the case when imaging biological samples. The supercontinuum employed is a SuperK Extreme EXR-9 (NKT Photonics A/S, Birkerød, Denmark) operating at a 320 MHz repetition rate. The supercontinuum is spectrally filtered to the range 1000 nm to 1750 nm to remove unwanted spectral components by applying a high- and a low-pass filter. The fiber coupler is TW1300R5A2 from Thorlabs, Inc. (USA), and the spectrometer is C-1070-1470-GL2KL (Wasatch Photonics, USA), which has 2048 pixels in the range 1070 nm to 1470 nm, giving an approximate pixel bandwidth of 0.2 nm. The spectrometer has a gain factor of  $\Delta e = 270$  electrons/count, specified by the manufacturer.

#### 3.1 Evaluating the excess noise

The average spectra for selected power levels are shown in Fig. 2(a), and the noise across the spectra is clearly visible. Fig. 2(b) shows the RIN calculated as in Eq. (2) for each pixel in the spectrometer and smoothed with a moving average window across 12.8 nm (64 pixels). This is compared to the RIN predicted by the old model,  $(\tau_c / \tau_p)^{1/2}$ , with 0.2 nm pixel bandwidth and  $\tau_p = 28$  ps estimated roughly from a simulation of the SuperK EXR-9 obtained by solving the generalized non-linear Schrödinger equation [6].

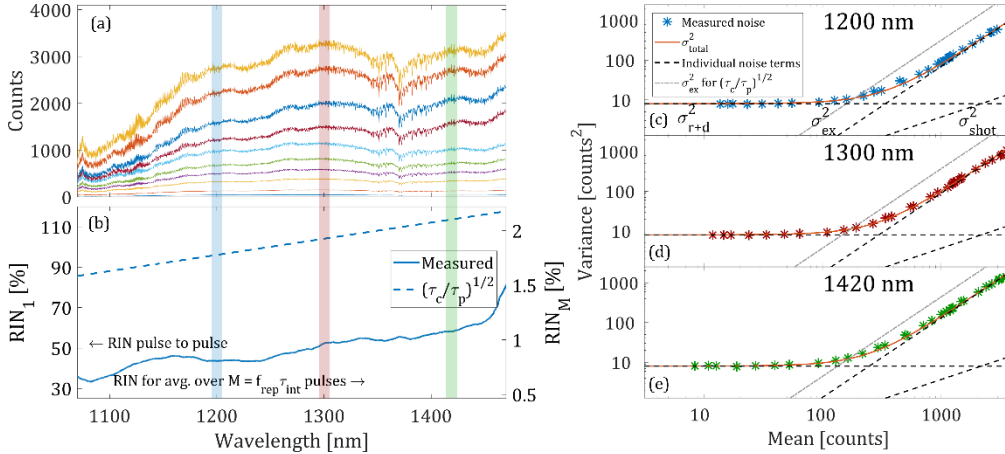


Fig. 2. (a) Mean spectra averaged over 1024 read-outs for selected power levels, (b) RIN calculated according to Eq. (2) using the series of spectra with the highest intensity in (a) and  $(\tau_c / \tau_p)^{1/2}$  from Eq. (6). (c)-(e) show the variance in counts versus the mean counts at 1200 nm, 1300 nm, and 1420 nm, respectively, within the spectral colored bands in (a) and (b).

The spectrometer is operated at an integration time  $\tau_i = 9.1 \mu\text{s}$ , giving  $M = 9.1 \mu\text{s} \times 320 \text{ MHz} = 2924$  detected pulses per read-out.  $RIN_M$  on the right y-axis are the measured values, and converted to the detector-independent  $RIN_1$  on the left axis by multiplication with  $\sqrt{M}$ . The prediction of the old model is on average 98 % higher in the detected spectral region than the measured RIN. This gives a 6 dB difference in sensitivity assuming excess noise

dominated imaging, which is not as bad as one might expect. Additionally, the slopes of the two RIN curves are very similar, posing the question whether in fact the old model is somehow valid for supercontinuum sources? The answer to this, we believe, is no. The RIN of the old model,  $(\tau_c/\tau_p)^{1/2}$ , will continue to decrease linearly with wavelength due to the  $\lambda^2$  dependence of  $\tau_c$ , whereas the supercontinuum RIN has a minimum at the pump wavelength (1064 nm in this case), and increases towards both sides of the spectrum [7,15]. Thus, at e.g. 800 nm, the measured RIN increases with decreasing wavelength, as opposed to the old model that predicts a decrease. The similarity observed here is thus attributed to chance. Figures 2(c)-(e) show the variance of counts versus the mean counts, at 1200 nm, 1300 nm, and 1420 nm respectively calculated for each pixel and averaged in 12.8 nm bands. The average is performed to achieve a better estimate for each point than is possible using a single pixel. The individual noise contributions are shown in dashed lines, with  $\sigma_{r+d}^2 = 8.1$  (fitted value) and  $\sigma_{shot}^2 = N_c/270$ . For the excess noise, the measurement-based prediction,  $\sigma_{ex}^2[i] = RIN_M[i]^2 N_c^2$ , is the black dashed line with the RIN values taken from solid line within the colored bands in Fig 2(b). The prediction of the old model, dashed in Fig. 2(b), is shown as the grey dash-dotted lines in Figs. 2(c)-(e), and we observe a clear deviation between the measured noise and the prediction of the old model. The total theoretical noise from the measurement-based model is plotted as the solid, red line, and we can immediately evaluate the accuracy of the excess noise predicted via the measured RIN. Furthermore, we notice that the shot noise surpasses the read-out and dark noise at  $\sim 2000$  counts, which means that even in the total absence of excess noise, the system would be limited by the read-out and dark noise when the reference signal alone reaches 50 % of the dynamic range (max. 4096 counts). The high read-out and dark noise is inherent to the InGaAs CCD detectors that are required for detecting in the 1300 nm region. In this case, the electronic noise is measured to be  $\sqrt{8.1} \approx 2.85$  counts RMS. Even 14 years ago, silicon CCDs were shown to exhibit electronic noise of  $\sim 0.55$  counts RMS allowing wider dynamic range for shot noise limited detection than modern InGaAs CCD detectors [23].

### 3.2 Spectral correlations and the OCT noise floor

Up until now, we have only considered the noise in  $k$ -space, but ultimately we are interested in the noise in the A-scan, i.e., in the  $z$ -domain. If we were dealing with white (uncorrelated) noise, the noise floor in the  $z$ -domain would be flat, and the specific level could be inferred directly by the variance in  $k$ -space, but unfortunately, supercontinuum excess noise is by no means white [3,17,19]. As discussed previously, the output of commercial supercontinuum sources consists of a sea of hundreds of individual solitons, which all make up the broadband spectrum. The solitons are very short in time and correspondingly wide in wavelength. Close to the pump, the pulse-to-pulse fluctuations arise due to the fact that the phase and central wavelength vary from soliton to soliton. As a result, several spectrally overlapping solitons will interfere, creating a chaotic spectrum with a seemingly random distribution of many narrowband peaks. Therefore, one pulse may have light at a certain wavelength while the next one may not. Integrating over enough pulses washes out these fluctuations, and the result is the flat and smooth spectrum often associated with supercontinua. If the supercontinuum is detected with a fast spectrometer, however, the noise becomes visible, as is the case in OCT. When the bandwidth of the light incident on a single pixel on the spectrometer is smaller than the bandwidth of the peaks created by soliton interference, the values of neighboring pixels become correlated, and the noise will then also be correlated. Computing and averaging an ensemble of autocorrelation functions for each acquired spectrum,  $I_{R,norm}$ , after standard OCT processing (background subtraction, normalization, and linearization), reveals any fixed patterns in the correlations. Such an average of autocorrelations,  $R(\Delta k) = \int_{-\infty}^{\infty} I_{R,norm}(k + \Delta k) I_{R,norm}(k) dk$ , for 500 spectra is shown in Fig. 3(a).

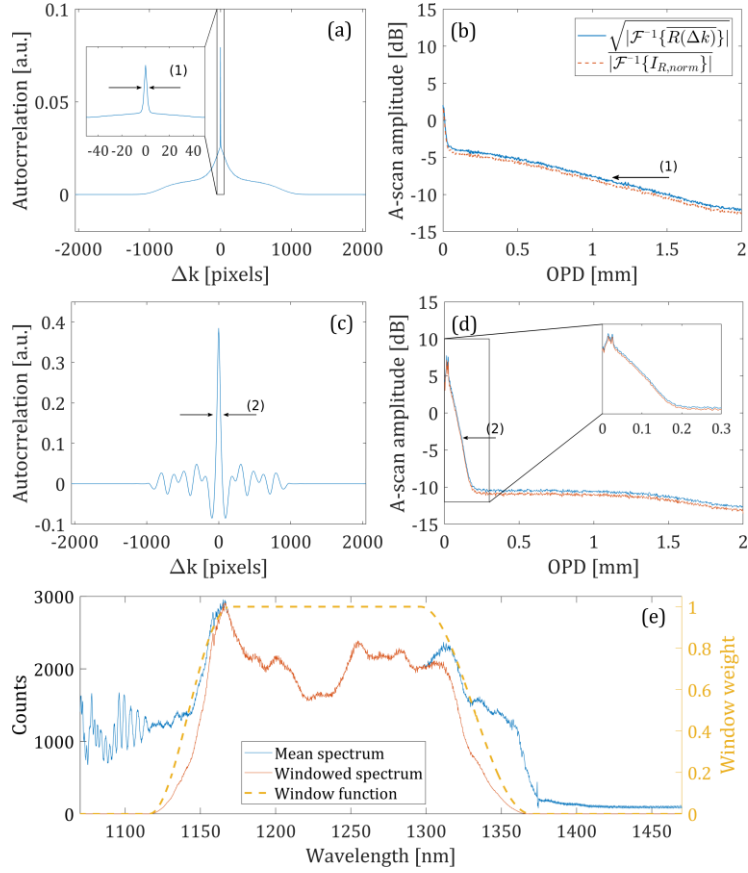


Fig. 3. Autocorrelations and noise floors for a conventional supercontinuum (a)-(b) and an ANDi supercontinuum (c)-(d). (a) Averaged autocorrelation for 500 OCT-processed spectra, and (b) averaged OCT noise floor (red) and the inverse Fourier transform of the autocorrelation in (a) (blue).  $\overline{\quad}$  denotes the ensemble average.

The narrow central part of the peak shown in the inset (marked by (1)) is caused by soliton interference, and its measured full-width at half-maximum of 3.8 pixels corresponds to an average soliton interference width between 0.5 and 0.6 nm at 1300 nm, well within the range of 0.1 to 1 nm coherence wavelength as suggested by Corwin et al. [16]. Figure 3(b) shows the OCT noise floor (average of 500 A-scans with blocked sample arm) in dashed red (bottom-most). The solid blue (top-most) curve shows the square root of the Fourier transform of the averaged autocorrelation of the same 500 spectra, and we see a good agreement, only a factor of  $\sim 0.5$  dB apart. Such an agreement is expected due to the Wiener-Khinchin theorem, which states that the autocorrelation function and the power spectral density (PSD) are linked through a Fourier transform [24]. Despite the name, the term PSD is not related to the spectral domain in general, this is only the case for temporal signals. The Wiener-Khinchin theorem holds between any two domains linked by a Fourier transform, and in OCT, the signal is detected in  $k$ -space, and the Wiener-Khinchin theorem thus links the autocorrelation in  $k$ -space with the PSD in the  $z$ -domain. The PSD in this case being the absolute square of the Fourier transform of  $I_{R, norm}$ , we expect to see perfect agreement between the two curves in Fig. 3(b), and that would indeed be the case if we were looking at a single spectrum. However, here we are dealing with averages of ensembles, and the 0.5 dB offset arises because the solid blue curve (top most curve) is the average of the autocorrelations, which is inherently proportional to the power

spectrum amplitude squared, whereas the dashed red curve is averaged over just the amplitude. Assuming Gaussian noise in  $k$ -space, both the real and imaginary part of the Fourier transform will also be Gaussian with variance  $\sigma^2(z)$ , where the  $z$ -dependence is due to the spectral correlations. The amplitude of the Fourier transform adheres to a Rayleigh distribution with mean  $\mu_R(z) = \sigma(z) \times \sqrt{\pi/2}$  [10]. The amplitude squared obeys a  $\chi^2$  distribution with  $k = 2$  degrees of freedom (a degree for each of the real and imaginary part), and the square root of the mean is  $(\mu_\chi(z))^{1/2} = \sigma(z) \times \sqrt{2}$ . This difference in probability distributions at the point of averaging gives rise to a factor of  $\mu_\chi^{1/2}/\mu_R = \sqrt{4/\pi} = 0.525$  dB between the two curves. Figures 3(c) and 3(d) show the same as Figs. 3(a) and 3(b), but for an ANDi supercontinuum generated by pumping a commercially available fiber with 165 fs pulses, see [25] for details. As the name suggests, the fibers used to generate ANDi supercontinua exhibit normal dispersion over the relevant wavelength range. This prohibits modulation instability and the formation of solitons, which are central to the generation of conventional supercontinua, and the generated supercontinuum consequently exhibits fundamentally different noise characteristics [26,27]. The extreme spectral broadening is caused by self-phase modulation and optical wave breaking, which are both coherent processes [26,28]. In the absence of solitons, the spectral components are correlated over a larger  $\Delta k$ , as seen by the peak in Fig. 3(c), marked by (2), which is significantly wider than the corresponding peak (1) in Fig. 3(a). These correlations contain the excess noise at optical path difference (OPD)  $< 200\mu\text{m}$ , leaving the noise floor at the remaining axial positions flat and low, seemingly shot noise dominated. The ripples observed in Fig. 3(c) are due to self-phase modulation, which creates fringes in the spectrum. Optical wave breaking subsequently washes out the fringes partially, and the ripples in Fig. 3(c) are the remnants of the self-phase modulation fringes. The ripples cause peak (2) in Fig. 3(d) to shift slightly away from OPD = 0, as it can be noticed from the inset in Fig. 3(d). This coherent noise stems from fluctuations in the pump. A varying pump peak power cause the self-phase modulation fringes to vary in both period and spectral extent, giving rise to spectrally coherent noise. For long pulses and/or long fiber lengths uncorrelated noise is also present because modulation instability is initiated in the orthogonal polarization (PMI) and the excellent coherence properties of the supercontinuum are lost. The limiting pulse and fiber lengths depend on both the birefringence of the ANDi fiber and the pulse peak power [29]. The 165 fs, 40 kW peak power, and 0.5 m fiber length used here suggests that we are at least partially in the PMI regime. The PMI noise is present across the entire axial range, and is thus difficult to distinguish from shot noise. Filtering away the coherent noise contribution at shallow OPD for each A-scan individually and returning via a Fourier transform to  $k$ -space, we obtain a variance of  $\sim 30$  counts squared per pixel, while the shot noise limited variance is expected to be  $N_c/\Delta e = 2000/270 = 7.4$ . The observed variance, and thus also the A-scan noise floor, is four times higher than the shot noise limit, allowing us to conclude that the PMI noise rather than the shot noise determines the noise floor amplitude at OPD  $> 200$  microns. The flat parts in Figs. 3(a) and 3(c) are due to the window applied (shown in Fig. (3(e)) to isolate the part of the ANDi spectrum that is useful for OCT. The window is also applied to the spectra from the conventional supercontinuum to ensure a fair comparison.

### 3.3 Assessing the sensitivity of supercontinuum-based OCT systems

Finally, the depth-dependent sensitivity of supercontinuum-based SD-OCT systems must be discussed. In OCT, the sensitivity is defined as the minimum sample reflectivity, which gives a signal-to-noise ratio (SNR) of 1 [9], and the sensitivity roll-off characterizes the signal degradation with the axial coordinate due to both finite pixel size and spectral resolution in the

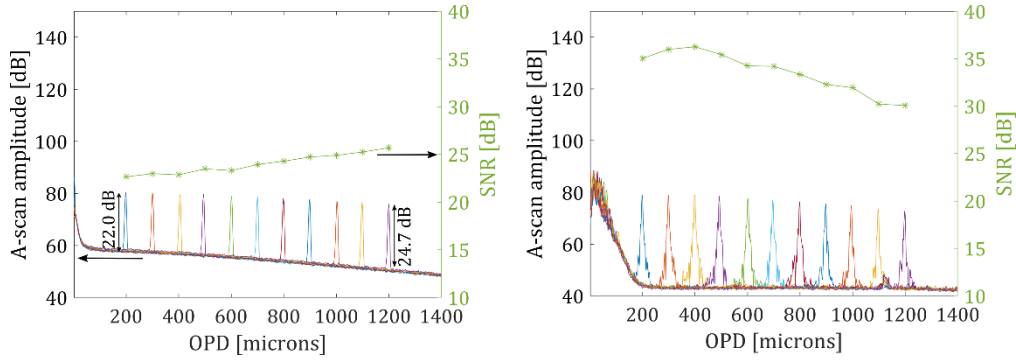


Fig. 4. Sensitivity of a supercontinuum-based SD-OCT system. Mean A-scan of a sample mirror at 11 different axial positions on the left axis, and the SNR on the right, for (a) a conventional supercontinuum, and (b) an ANDi supercontinuum.

spectrometer [30]. The shape of the noise floor is typically not included in the roll-off because most OCT systems employing non-supercontinuum sources are shot noise limited, and thus exhibit white noise characteristics [9,19,31]. The sensitivity figure for a given system is then evaluated at a shallow axial coordinate value, where the signal, and thereby also the sensitivity, is larger. However, for a supercontinuum-based SD-OCT, the noise floor decreases with axial position, and this impacts both the sensitivity figure and the roll-off. To illustrate this point, Fig. 4 shows the mean amplitude on the left axis calculated for 500 A-scans for each mirror position at 11 different axial positions in the sample arm as well as the SNR on the right axis. In Fig. 4(a), a conventional supercontinuum is used, and in (b) an ANDi supercontinuum. For the conventional supercontinuum in Fig. 4(a), we notice a signal roll-off of 6.4 dB from 200  $\mu\text{m}$  to 1200  $\mu\text{m}$ , characteristic to SD-OCT, but the decrease of the noise floor is larger at 9 dB, yielding a SNR *increase* along the axial coordinate. For the ANDi supercontinuum, however, the SNR decreases with depth, after reaching a maximum at  $\sim 400\mu\text{m}$  OPD. The sensitivity figure for the system should thus not by default be the sensitivity at shallow depth, but rather the maximum sensitivity over the entire range.

#### 4. Conclusion

In conclusion, we have developed an assumption-free model for the excess noise of a supercontinuum source based on the measured amplitude fluctuations and shown that it predicts the measured noise extremely well. The excess noise can be reduced by increasing either the integration time of the spectrometer or the pulse repetition rate of the supercontinuum, but even without excess noise, truly shot noise limited performance may be difficult to achieve at 1300 nm due to the high electronic noise of InGaAs CCDs. This forces using a higher optical power, to exceed the readout noise, to a value where the excess photon noise exceeds the shot noise. The spectral correlations of the supercontinuum determine the shape of the noise floor, which is not flat versus OPD. A commercially available conventional supercontinuum source, as well as an in-house built ANDi supercontinuum source, were used to investigate different types of correlations and their effect on the noise floor. The conventional supercontinuum is spectrally correlated over only sub-nm wavelength differences due to interference of hundreds of optical solitons, which gives a relatively high but decreasing noise floor in the A-scan. The ANDi supercontinuum, however, is correlated across several nm due to the inherent coherence of self-phase modulation and optical wave breaking, which contains the RIN noise of the ANDi supercontinuum at axial positions close to 0 OPD in the A-scan, thus leaving the remaining axial positions limited by the incoherent noise from polarization modulation instability, whose impact depends on pump and fiber parameters. The shape of the noise floor must therefore be

taken into account when characterizing the sensitivity and roll-off of a supercontinuum-based SD-OCT system.

## Acknowledgements

M. Jensen, N.M. Israelsen, R.D. Engelsholm, O. Bang and A. Podoleanu acknowledge support from Innovation Fund Denmark through the ShapeOCT grant No. 4107-00011A. Marie Curie EID UBAPHODESA FP7-PEOPLE-2013-ITN 607627 supports M. Maria, and A. Podoleanu, the UCL Institute of Ophthalmology and the Royal Society Wolfson Research Merit Award also supports A. Podoleanu. O. Bang and M. Maria acknowledge support from the Horizon 2020 grant GALAHAD (project no. 732613). I.B. Gonzalo and O. Bang are supported by the Independent Research Fund Denmark (DFR), through grant LOISE-4184-00532B.

## References

1. D. Huang, E. A. Swanson, C. P. Lin, J. S. Schuman, W. G. Stinson, W. Chang, M. R. Hee, T. Flotte, K. Gregory, C. A. Puliafito, and J. G. Fujimoto, "Optical coherence tomography," *Science* (80-. ). **254**(5035), 1178–81 (1991).
2. D. J. Harper, M. Augustin, A. Lichtenegger, P. Eugui, C. Reyes, M. Glösmann, C. K. Hitzenberger, and B. Baumann, "White light polarization sensitive optical coherence tomography for sub-micron axial resolution and spectroscopic contrast in the murine retina," *Biomed. Opt. Express* **9**(5), 2115–2129 (2018).
3. X. Yao, Y. Gan, C. C. Marboe, and C. P. Hendon, "Myocardial imaging using ultrahigh-resolution spectral domain optical coherence tomography," *J. Biomed. Opt.* **21**(6), 061006 (2016).
4. W. Yuan, J. Mavadia-Shukla, J. Xi, W. Liang, X. Yu, S. Yu, and X. Li, "Optimal operational conditions for supercontinuum-based ultrahigh-resolution endoscopic OCT imaging," *Opt. Lett.* **41**(2), 250 (2016).
5. N. M. Israelsen, M. Maria, M. Mogensen, S. Bojesen, M. Jensen, M. Haedersdal, A. Podoleanu, and O. Bang, "The value of ultrahigh resolution OCT in dermatology - delineating the dermo-epidermal junction , capillaries in the dermal papillae and vellus hairs," *Biomed. Opt. Express* **9**(5), 958–963 (2018).
6. J. M. Dudley, G. Genty, and S. Coen, "Supercontinuum generation in photonic crystal fiber," *Rev. Mod. Phys.* **78**(4), 1135–1184 (2006).
7. U. Møller, S. T. Sørensen, C. Jakobsen, J. Johansen, P. M. Moselund, C. L. Thomsen, and O. Bang, "Power dependence of supercontinuum noise in uniform and tapered PCFs," *Opt. Express* **20**(3), 2851–2857 (2012).
8. D. R. Solli, C. Ropers, P. Koonath, and B. Jalali, "Optical rogue waves," *Nature* **450**(7172), 1054–1057 (2007).
9. R. A. Leitgeb, C. K. Hitzenberger, and A. F. Fercher, "Performance of fourier domain vs. time domain optical coherence tomography," *Opt. Express* **11**(8), 889–894 (2003).
10. J. W. Goodman, *Statistical Optics*, 1st ed. (John Wiley & Sons, Inc., 1985).
11. B. M. Hoeling, A. D. Fernandez, R. C. Haskell, E. Huang, W. R. Myers, D. C. Petersen, S. E. Ungersma, R. Wang, M. E. Williams, and S. E. Fraser, "An optical coherence microscope for 3-dimensional imaging in developmental biology," *Opt. Express* **6**(7), 136–146 (2000).
12. W. Drexler and J. H. Fujimoto, eds., *Optical Coherence Tomography Technology and Applications*, 2nd ed. (Springer International Publishing, 2015).
13. S. Shin, U. Sharma, H. Tu, W. Jung, and S. A. Boppart, "Characterization and Analysis of Relative Intensity Noise in Broadband Optical Sources for Optical Coherence Tomography," *IEEE Photonics Technol. Lett.* **22**(14), 1057–1059 (2010).
14. C. Lafargue, J. Bolger, G. Genty, F. Dias, J. M. Dudley, and B. J. Eggleton, "Direct detection of optical rogue wave energy statistics in supercontinuum generation," *Electron. Lett.* **45**(4), 217–219 (2009).
15. A. Kudlinski, B. Barvian, A. Leray, C. Spriet, L. Hélot, and A. Mussot, "Control of pulse-to-pulse fluctuations in visible supercontinuum," *Opt. Express* **18**(26), 27445–27454 (2010).
16. K. L. Corwin, N. R. Newbury, J. M. Dudley, S. Coen, S. A. Diddams, B. R. Washburn, K. Weber, and R. S. Windeler, "Fundamental amplitude noise limitations to supercontinuum spectra generated in a microstructured fiber," *Appl. Phys. B Lasers Opt.* **77**(2–3), 269–277 (2003).
17. M. Maria, I. Bravo Gonzalo, T. Feuchter, M. Denninger, P. M. Moselund, L. Leick, O. Bang, and A. Podoleanu, "Q-switch-pumped supercontinuum for ultra-high resolution optical coherence tomography," *Opt. Lett.* **42**(22), 4744–4747 (2017).
18. S. T. Sørensen, O. Bang, B. Wetzel, and J. M. Dudley, "Describing supercontinuum noise and rogue wave statistics using higher-order moments," *Opt. Commun.* **285**(9), 2451–2455 (2012).
19. W. J. Brown, S. Kim, and A. Wax, "Noise characterization of supercontinuum sources for low-coherence interferometry applications," *J. Opt. Soc. Am. A* **31**(12), 2703 (2014).
20. P. R. Morkel, R. I. Laming, and D. N. Payne, "Noise characteristics of high-power doped-fibre superluminescent sources," *Electron. Lett.* **26**(2), 96 (1990).

21. A. G. Podoleanu, "Unique interpretation of Talbot Bands and Fourier domain white light interferometry," *Opt. Express* **15**(15), 9867 (2007).
22. N. Nassif, B. Cense, B. Hyle Park, S. H. Yun, T. C. Chen, B. E. Bouma, G. J. Tearney, and J. F. de Boer, "In vivo human retinal imaging by ultrahigh-speed spectral domain optical coherence tomography," *Opt. Lett.* **29**(5), 480–482 (2004).
23. N. A. Nassif, B. Cense, B. H. Park, M. C. Pierce, S. H. Yun, B. E. Bouma, G. J. Tearney, T. C. Chen, and J. F. de Boer, "In vivo high-resolution video-rate spectral-domain optical coherence tomography of the human retina and optic nerve," *Opt. Express* **12**(3), 367 (2004).
24. J. G. Proakis and D. G. Monolakis, *Digital Signal Processing*, 4th ed. (Pearson, 2007).
25. I. B. Gonzalo, M. Maria, R. D. Engelsholm, T. Feuchter, L. Leick, P. M. Moselund, A. Podoleanu, and O. Bang, "Ultra-low noise supercontinuum source for ultra-high resolution optical coherence tomography at 1300 nm," in *Progress in Biomedical Optics and Imaging - Proceedings of SPIE* (2018), **10486**.
26. A. M. Heidt, J. S. Feehan, J. H. V. Price, and T. Feurer, "Limits of coherent supercontinuum generation in normal dispersion fibers," *J. Opt. Soc. Am. B* **34**(4), 764–775 (2017).
27. M. Klimczak, G. Soboń, R. Kasztelanic, K. M. Abramski, and R. Buczyński, "Direct comparison of shot-to-shot noise performance of all normal dispersion and anomalous dispersion supercontinuum pumped with sub-picosecond pulse fiber-based laser," *Sci. Rep.* **6**(1), 19284 (2016).
28. C. Finot, B. Kibler, L. Provost, and S. Wabnitz, "Beneficial impact of wave-breaking for coherent continuum formation in normally dispersive nonlinear fibers," *J. Opt. Soc. Am. B* **25**(11), 1938–1948 (2008).
29. I. B. Gonzalo, R. D. Engelsholm, M. P. Sørensen, and O. Bang, "Polarization noise places severe constraints on coherence of all-normal dispersion femtosecond supercontinuum generation," *Sci. Rep.* **8**(1), 1–13 (2018).
30. S. Yun, G. Tearney, B. Bouma, B. Park, and J. de Boer, "High-speed spectral-domain optical coherence tomography at 13  $\mu\text{m}$  wavelength," *Opt. Express* **11**(26), 3598 (2003).
31. J. F. de Boer, B. Cense, B. H. Park, M. C. Pierce, G. J. Tearney, and B. E. Bouma, "Improved signal-to-noise ratio in spectral-domain compared with time-domain optical coherence tomography," *Opt. Lett.* **28**(21), 2067 (2003).